RESEARCH ARTICLE | APRIL 01 2024

Atomic hydrogen production in a cold plasma for application in a metal foil pump

Yannick Kathage ; Stefan Hanke ; Thomas Giegerich ; Christian Day

Phys. Plasmas 31, 043503 (2024)
https://doi.org/10.1063/5.0190210

Atomic hydrogen production in a cold plasma for application in a metal foil pump

Cite as: Phys. Plasmas **31**, 043503 (2024); doi: 10.1063/5.0190210
Submitted: 4 December 2023 · Accepted: 3 March 2024 ·
Published Online: 1 April 2024

Yannick Kathage,[a] Stefan Hanke, Thomas Giegerich, and Christian Day

AFFILIATIONS

Karlsruhe Institute of Technology (KIT), 76131 Karlsruhe, Germany

[a]Author to whom correspondence should be addressed: yannick.kathage@kit.edu

ABSTRACT

Any good design of fuel cycles for thermonuclear fusion reactors, which operate on deuterium-tritium fusion, comes with minimized tritium inventory. The direct internal recycling concept can significantly reduce the tritium inventory of a fusion power plant by introducing a bypass for most of the unburned fuel from the torus exhaust. It requires a technology that can sharply separate hydrogen isotopes from other gases in the given environment in the reactor's pump duct. The prime candidate for this task is a metal foil pump (MFP) using plasma-driven permeation. A workflow toward a performance predicting modeling tool of a MFP is introduced. It is based on the characterization of the employed cold plasma by using a plasma simulation, which is experimentally validated using optical emission spectroscopy and the actinometry method. The used approach accounts for the radial inhomogeneity of the linearly extended plasma. We determine the atomic hydrogen content down to pressures of 1 Pa and condense the complex processes that contribute to the hydrogen atom production into a single excitation probability. This value can be used in Monte Carlo based modeling approaches to determine the particle exhaust performance of the vacuum pump.

I. INTRODUCTION

The aim of reducing the tritium inventory in the next generation fusion power plants, namely, DEMO, has turned out to be a strong driver for the development of new, alternative fuel cycle technologies.[1] Such can be found in the concept of Direct Internal Recycling (DIR) as proposed by KIT.[2] It foresees bypassing of the tritium plant for a large fraction of unburnt fuels. Those are separated from the torus exhaust close to the divertor and recycled to the matter injection systems.[3] In another loop, only the non-recycled part of the exhaust gas is routed through the tritium plant systems, where the removal of protium, helium, and plasma-enhancement gases (PEGs) from the fuel is being undertaken. Owing to the reduction of the process flows, the processing systems can be scaled down, lowering their tritium inventories. The average tritium recycling time also decreases immensely due to the introduced short-cut for the fuel.[4]

The prime candidate to fulfill the fuel separation duty is the metal foil pump (MFP), which uses superpermeation. In Ref. 5, superpermeability is associated with the requirement of a source of atomic hydrogen and a thin metal foil with a nonmetallic impurity monolayer on its surface. The atomic hydrogen has high probabilities for absorption into the metal, while the impurity layer inhibits the absorption of hydrogen impinging in the molecular form.[6] The hydrogen diffuses to the downstream surface, where it can recombine and be released into the gas-phase again.[7] Our research focuses on the interaction of a cylindrical, surface-wave sustained microwave plasma source[8] with pure group 5 metal foils made from Nb and V. Next to industrial availability, the plasma source type offers good scalability and high power densities to achieve separation of large fluxes in the available space in the DEMO pump duct.

As part of our development plan, several MFP designs are investigated in view of their ability to pump and separate hydrogenic species and offer large conductance during the dwell phase. This evaluation succeeds in a performance predicting modeling tool based on the Test Particle Monte Carlo (TPMC) approach, which uses the free molecular flow code ProVac3D.[9] It allows testing of complex geometries with reasonable computational effort, much lower than that of Direct Simulation Monte Carlo (DSMC) approaches. To this end, all relevant processes taking place in the plasma volume are condensed into a not physically accessible parameter, the plasma excitation probability. It is defined as the probability of a surface reaction that turns an impinging hydrogen molecule into an atom, not accounting for mass balance, and is exclusive to the plasma source boundary. By evaluating plasma

excitation probabilities that yield atomic hydrogen fractions corresponding to the plasma simulation for a specific volume at certain operation conditions, the complexity of simulating large plasmas in the geometries of the MFP by DSMC approaches is avoided.

An exemplary sketch of a MFP design is given in Fig. 1 to explain the boundary conditions in the TPMC simulation. For the simulation of the burn phase, a large number of ground-state particles, namely, D_2 molecules, enter the MFP through the inlet. Running the model requires knowledge of parameters that describe the interaction of the relevant particles with the boundaries. Specific interactions with respective probabilities will have to be prescribed to the boundaries, most importantly reflection, excitation, and de-excitation on the plasma boundary and permeation through the foil boundary.

Permeation probabilities can be found in the literature.[5,6] Excitation transforms the ground-state particle to an excited particle with the ability to permeate through the foil like a hydrogen atom. Thus, excited is used equivalently to atomic hydrogen here. Assuming the excited particle in the TPMC simulation is atomic hydrogen, its de-excitation can be understood as surface recombination, for which probabilities are given in the literature.[10–12]

The TPMC simulation models only one particle at a time. Thus, in our simplified approach, the excitation of one ground-state particle only transforms it to one excited particle, not accounting for mass balance of the dissociation and recombination reactions. To obtain the excitation probability, first, the plasma needs to be characterized.

We approach the issue by validating the simulation and finding an excitation probability, which yields volume-averaged atomic hydrogen molar fractions corresponding to those in the plasma in our experimental setup HERMES*plus*. Figure 2 describes the workflow to come to this value, using a 2D axisymmetric hydrogen plasma simulation as a link between experiment and TPMC simulation. The experimentally obtained atomic hydrogen molar fraction measurements are compared against what the simulation predicts for the individual measurements. We build a simplified model of the plasma simulation with only ground-state and excited species and identical boundary conditions except for the plasma source boundary, which is prescribed an excitation probability. By evaluating the volume-averaged atomic hydrogen molar fraction for varying pressure and plasma power, we match excitation probabilities to plasma source operation points for use in the Monte Carlo model. The TPMC simulation also features a foil boundary, through which the excited particles can permeate with a probability depending on findings from experiment and literature. This probability also considers the effective change in the permeation flux due to the presence of noble gases.

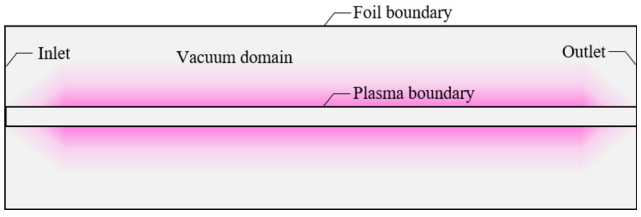

FIG. 1. Model of cylindrical MFP used in the Test Particle Monte Carlo simulation.

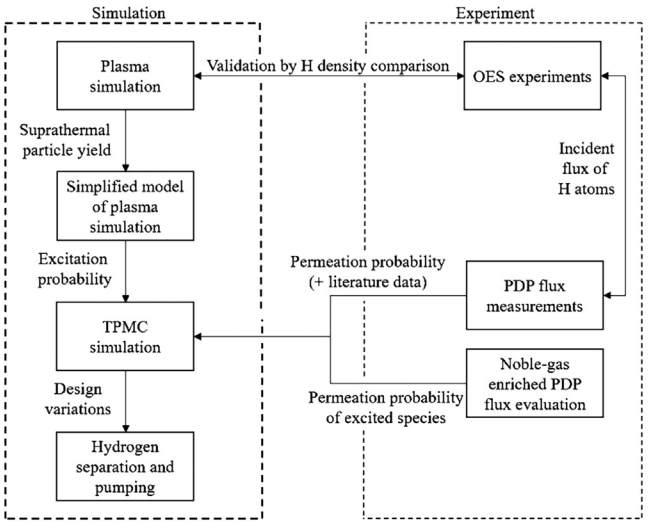

FIG. 2. Workflow toward a performance predicting modeling tool for a MFP.

II. EXPERIMENTAL METHOD

The experimental method we use to evaluate the atomic hydrogen concentration is referred to as actinometry.[13–15] It allows for the estimation of the ground-state density of a species A (here, H) based on the knowledge of the density of another ground-state species B (here, Ar) and optical emission spectroscopy (OES). In plasma, both ground-state species are excited to a certain excited state via direct electron impact with a rate $k_{r,i}$. This state radiatively decays, emitting photons of a characteristic wavelength detected spectroscopically. For the method to be accurate, the excitation to the radiative state has to predominantly happen from the ground-state and not in two-step processes. The de-excitation has to occur through mainly radiative decay. Furthermore, the excitation threshold for the two species should be similar, and the cross sections should exhibit similar shapes. Given those conditions, the densities of the species follow the simple relationship

$$\frac{n_A}{n_B} = k\frac{I_A}{I_B}, \tag{1}$$

in which n_A and n_B are the two respective ground-state atom densities, k is a constant, and I_A and I_B are the intensities at the two characteristic wavelengths of de-excitation of the excited states of species A and B, respectively.

Ar has been used extensively in the literature as actinometer for the measurement of the atomic hydrogen concentration.[13,14] Due to their strong signal and similar excitation thresholds and cross sections for the production of the emitting states, the H-α line (656.28 nm) and the Ar($2p_1 \rightarrow 1s_2$) line (750.387 nm) are chosen for the evaluation. In this experiment, shown in a scheme in Fig. 3, hydrogen plasma is seeded with a small amount of Ar, of which the neutral ground-state density is known precisely. The introduced amount must not impact the hydrogen plasma significantly. Considering the respective feeds through calibrated mass flow controllers and the previously determined pumping speeds for H and Ar, we calculate the gas composition in the vessel. In our plasma, high degrees of dissociation are given,

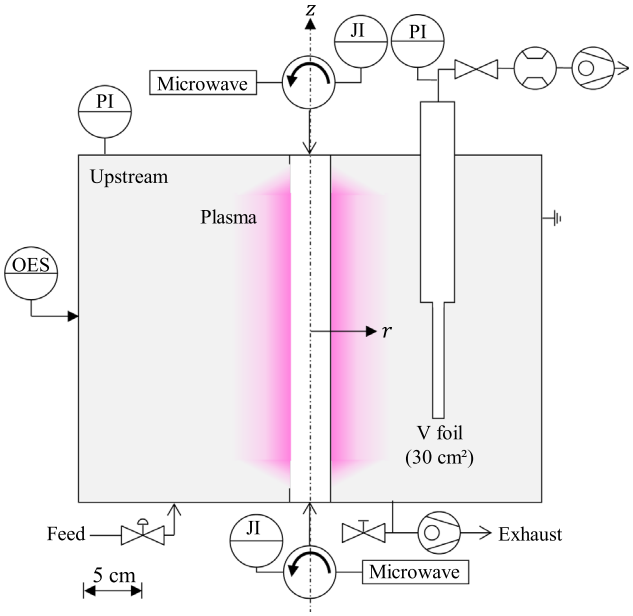

FIG. 3. HERMES*plus* plasma vessel.

leading to an increase in pressure when switching on the plasma. To keep the pressure steady, the valve to pumping is opened correspondingly, decreasing the molar fraction of Ar. When calculating the desired feed ratio to reach a certain Ar concentration, we take the measured feed ratio to obtain the same pressure in the vessel at a given valve position with the individual H and Ar feeds. Considering free molecular flow through the small opening of the valve in front of the turbomolecular pump, one would expect a required flow ratio of the square-root of the mass ratio of H_2 and Ar, i.e. $(2/40)^{0.5} = 0.224$ to achieve the same partial pressure of the two gases. We experimentally determine a feed ratio of 0.2233 for H_2 and Ar, which is roughly 0.224 and within the uncertainties of the flow meters. However, dissociating a large fraction of hydrogen changes the situation as the pumping speed of H is greater than that of H_2. Taking a first guess for the volume-averaged atomic hydrogen concentration from the simulation y_H, we can compute a pumping speed ratio of Ar/H pumping during plasma,

$$s_{mix} = y_H \left(\frac{1}{40}\right)^{0.5} + (1 - y_H)\left(\frac{2}{40}\right)^{0.5}. \tag{2}$$

Considering the feed flows $\dot{F}$ of H_2 and Ar, the concentration of Ar can be computed with a correction for the relative increase in H particles due to dissociation, introduced by the factor g_H,

$$y_{Ar} = \frac{1}{\frac{\dot{F}_H}{\dot{F}_{Ar}} s_{mix} g_H} = \frac{1}{\frac{\dot{F}_H}{\dot{F}_{Ar}} s_{mix} \frac{1}{(1 - 0.5 y_H)}}. \tag{3}$$

The main vessel is continuously pumped by a Pfeiffer TPU 180 H turbomolecular pump with two Leybold Ecodry 25 plus roots pumps in parallel as roughing pumps. As shown in Fig. 3, the main vessel is connected to the chamber downstream the metal foil via a bypass that is opened during the experiment. A gate valve stops pumping in the downstream chamber so that selective hydrogen pumping by the semi-permeable foil does not impact the hydrogen concentration in the vessel. Hence, pumping of H and Ar only occurs on the main vessel.

The measurements are performed within our experimental setup HERMES*plus*, which features a 2.45 GHz microwave plasma source at its center with 4 kW maximum power and a 0.1 mm thick, 30 cm^2 vanadium foil at a radial distance of ~100 mm to said plasma source. Reflected microwave power is measured and deposited in a dummy load by a circulator. The foil is of tubular shape and open toward one end, to which the downstream chamber is connected. The upstream pressure is measured using a Leybold capacitance manometer CM 1 and a MKS Instruments 690A Baratron gauge, which were in reasonably good agreement with each other. The setup is equipped with a Plasus EMICON SA optical emission spectroscope (200–1100 nm with a resolution of 1.5 nm) with a collimator optic installed with a radial view on the plasma column ex-vacuum. It can be manually adjusted to probe the plasma at different angles.

The constant k from Eq. (1) constitutes from several different factors as taken from[13]

$$k = FQ\frac{k_{r,Ar}}{k_{r,H}}, \tag{4}$$

in which F takes into account the optical device response K_i at the different wavelengths, the radiative decay rate $k_{rad,i}$ at which the measured line is emitted of species as well as the total radiative decay rate of the excited species $k_{rad,i,tot}$ and the wavelength λ_i,

$$F = \frac{K_{Ar}\lambda_H \frac{k_{rad,Ar}}{k_{rad,Ar,tot}}}{K_H \lambda_{Ar} \frac{k_{rad,H}}{k_{rad,H,tot}}}. \tag{5}$$

The factor Q is a term that considers all of the quenching reactions that destroy the emitting excited state of Ar and H.[13] We only consider quenching reactions of the excited species with H, H_2, and Ar. The quenching reaction rates are obtained from the relative collision velocity, which is the average of the thermal velocities of the two colliding species.

The reaction rates for ground-state excitation by direct electron impact $k_{r,i}$ are calculated assuming a generalized approach for the electron energy distribution function (EEDF)[16,17] using the relationship

$$k_{r,i} = \sqrt{\frac{2}{m_e}} \int_0^\infty \sigma_i(\epsilon)\epsilon f(\epsilon) d\epsilon, \tag{6}$$

with m_e being the electron mass, $\sigma_i(\epsilon)$ the collisional cross section to produce the emitting state, which is a function of the electron energy ϵ, and $f(\epsilon)$ the EEDF in $eV^{-1.5}$. The power law of the generalized EEDF is obtained from a linear function of the electron mean energy in the respective plasma region. Abel's inversion cannot be employed to our setup due to geometric constraints of our plasma vessel.

The choice of EEDF significantly impacts the determined reaction rates of the two reactions in Eq. (4), which can lead to substantially different results. We compute the EEDF with a generalized approach, being neither pure Maxwellian' nor pure Druyvesteyn', but instead a mix of the two. In publications on actinometry, often a Maxwellian

EEDF is assumed to compute the reaction rates.[13,14] The Maxwellian' is a simplified form of the Boltzmann distribution, which assumes thermodynamic equilibrium as is usually the case when the ionization degree is high. However, this typically does not apply to cold plasma like the one in the present work, which exhibits non-Maxwellian behavior. The Druyvesteyn' EEDF, on the other hand, was specifically derived to describe cold plasma like in industrial or laboratory applications.[18] In comparison to the Maxwellian' EEDF, it not only exhibits a shift of the maximum of the EEDF toward higher energies for one electron mean energy but also leads to lower population of the high energy tail of the EEDF corresponding to fast losses of the fast electrons to the surrounding walls.[19] We assume our plasma to be close to Maxwellian' in the center of the plasma vessel and close to Druyvesteyn' at the outer walls of the vessel. This radial shift in the EEDF is implemented by calculating the power law of the generalized EEDF as a function of the electron mean energy. This fit function comes from a first solution of the whole system for the operation point of 20 Pa and 2.4 kW plasma power, for which a good match between simulation and experiment is obtained. The same fit function is applied to all the measurements for consistency of the validation approach.

A novelty in our experiment is that we do not compute the reaction rate based on the most active plasma region but instead divide the axisymmetric plasma in rings, for which we compute $k_{r,i}$ individually. For the evaluation of the EEDF and reaction rates $k_{r,i}$, we also consider the presence of Ar with the corresponding molar fractions from the experiment and the respective plasma chemistry but without H–Ar collisions.

We use a first solution from simulation to approximate the local plasma composition and electron temperature and density in the individual rings at the axial position of the line of sight. Figure 4 shows their segmentation and two of the OES' lines-of-sight for experiments, for which the integral intensity ratio of the two characteristic lines is obtained. The line-of-sight angle is β. A perfect mixture is assumed, yielding a homogeneous Ar concentration throughout the vessel. Based on the length of the line of sight through each ring, we use weighing factors to compute an average reaction rate for each measurement. Thus, the average reaction rate $k_{r,i,j}$ that applies to a measurement j is obtained by summing over rings $q = 1$–12 according to

$$k_{r,i,j} = \sum_{q=1}^{12} \frac{l_q}{l_{tot,j}} k_{r,i,q}. \tag{7}$$

In the same fashion, the average particle densities and quenching reaction rates for the respective measurement are computed.

A schematic of the simulation domain is given in Fig. 5. It features a 2D axisymmetric model of the experimental setup HERMES*plus* with inner and outer conductors, cooling air channel, and dielectric and plasma domain. A time-harmonic, electromagnetic wave (2.45 GHz) in transverse electromagnetic mode is fed from two opposing ports, entering the vacuum domain through a dielectric window to perform work on an electron fluid in the plasma domain. While the fluid approximation makes the problem computationally much less demanding, it becomes inaccurate at too low pressures.[17] It allows describing the electron fluid with macroscopic quantities such as the electron density, mean electron energy, and mean electron momentum as done by using the *Microwave Plasma* and *Electromagnetic Wave* interfaces of the COMSOL Multiphysics software. The equations that describe the quantities are obtained from the Boltzmann equation by averaging over velocity space. In this way, the emerging distribution functions only depend on space and time.[18] Neglecting the neutral fluid velocity, this approach gives rise to the so-called continuity equation

$$\frac{\partial n_e}{\partial t} + \nabla \cdot (n_e \boldsymbol{u}_e) = S_e - L_e, \tag{8}$$

where n_e is the electron density, $\boldsymbol{u}_e$ is the electron drift velocity, and S_e and L_e are the source and loss term of electrons, respectively. This equation is typically used to describe the electron balance for each element of a simulation domain, in which the electron movement over

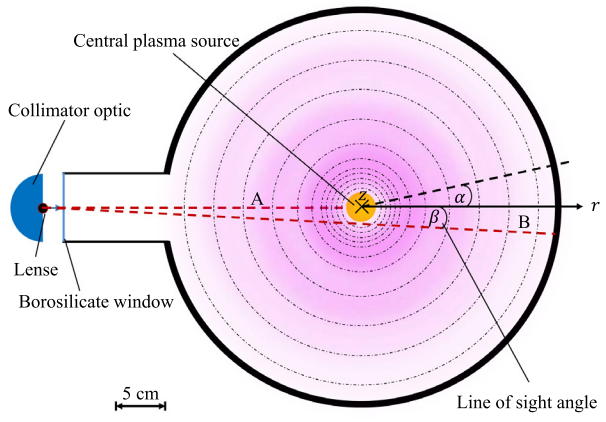

FIG. 4. Ring segmentation for OES measurements of atomic hydrogen concentration and lines of sight of spectroscope.

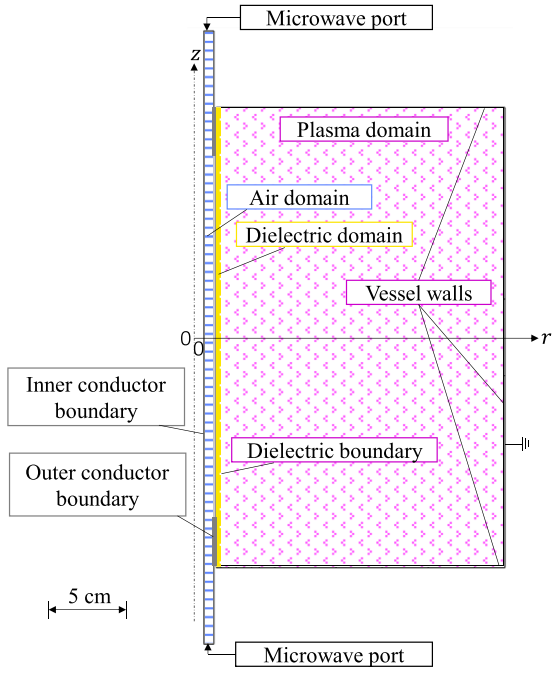

FIG. 5. Model of the plasma vessel in the simulation.

the cell boundaries is given by the second term. The right-hand side of the equation is defined by the plasma chemistry.

Our chemistry considers several different ionization reactions and only a few volume recombination reactions. Most electrons are lost to the walls, for which an additional set of reactions is considered. The vessel walls, like in the experimental setup HERMES*plus*, are grounded, and no charge accumulation occurs. However, we consider secondary electron emission by electrons and some heavy species with probabilities taken from literature.[21,22] The source term can then be expressed as

$$S_e = \sum_{m=1}^{n} y_H n_e n_H k_{r,m}, \tag{9}$$

where $y_H n_H$ defines the number density of the heavy species H that participates in the ionizing reaction for all n ionizing reactions. The energy density of a plasma without superimposed bulk velocity of the gas can be described through the expression

$$\frac{\partial n_\varepsilon}{\partial t} + \nabla \cdot \boldsymbol{\Gamma}_\varepsilon + \boldsymbol{E} \cdot \boldsymbol{\Gamma}_e = G_e + \frac{P}{q}, \tag{10}$$

where n_ε is the electron energy density, $\boldsymbol{\Gamma}_\varepsilon$ is the electron energy flux, $\boldsymbol{E}$ is the electric field arising from charge separation, G_e is the energy gain or loss in the respective volume, and P is the power density transferred to the electron fluid by the microwave. The energy loss in the volume is, again, defined by the assigned plasma chemistry through the relation

$$G_e = \sum_{m=1}^{n} y_H n_e n_H k_{r,i} \Delta\varepsilon_m, \tag{11}$$

with the energy loss $\Delta\varepsilon_m$ for reaction m. The macroscopic quantity of momentum conservation allows for solving for the electron flux

$$\boldsymbol{\Gamma}_e = \boldsymbol{u}_e n_e \tag{12}$$

using the assumptions that the momentum exchange frequency is significantly larger than the frequencies of the microwave, ionization, or attachment reactions. Additionally, if the thermal velocity of electrons is much larger than the electron drift velocity $\boldsymbol{u}_e$, it can be formulated as[20]

$$\boldsymbol{u}_e = \frac{q}{m_e \nu_m}\boldsymbol{E} - \frac{k_B}{m_e \nu_m}\nabla T_e - \frac{k_B T_e}{n_e m_e \nu_m}\nabla n_e, \tag{13}$$

with ν_m being the frequency for momentum transfer collisions, m_e the electron mass, k_B Boltzmann's constant, and T_e the electron temperature.

To help buildup of plasma, an initial electron density of $n_{e,0} = 10^{16}\ \mathrm{m}^{-3}$ is assumed. A simplified form of the wave equation is solved in the frequency domain. The microwave's time-varying electric field $\bar{\boldsymbol{E}}_m$ resistively heats the electron fluid by inducing a current density of amplitude $\bar{\boldsymbol{J}}$ according to

$$P = \frac{1}{2} Re\left(\bar{\boldsymbol{J}} \cdot \bar{\boldsymbol{E}}_m^{\circ}\right) = \frac{1}{2}|\bar{\boldsymbol{E}}_m|^2 Re(\sigma), \tag{14}$$

in the electron fluid that is described by its electrical conductivity

$$\sigma = \frac{n_e e^2}{m_e(\nu_m + j\omega)}, \tag{15}$$

where e is the electron space charge and $\bar{\boldsymbol{E}}_m^{\circ}$ is the complex conjugate of the microwave's electric field.[17]

The heavy species diffusion is modeled using a simplified form of the Maxwell-Stefan equation,[23] which assumes a mixture-averaged diffusion coefficient D_{ij} based on the respective mass fractions of all heavy species w_i.[17] The diffusion of species i to n in a multicomponent fluid can be described assuming a local equilibrium of the thermodynamical driving force and the total friction force experienced by this species according to

$$\frac{y_i}{RT}\nabla\mu_i = -\sum_{j\neq 1}^{n} \frac{x_j \boldsymbol{J}_{M,i} - x_i \boldsymbol{J}_{M,j}}{c_{tot} D_{ij}} \quad for\ i = 1 \ldots n, \tag{16}$$

where R is the universal gas constant, μ_i is the chemical potential, $\boldsymbol{J}_M$ is the diffusive molar fluxes, and D_{ij} is the binary Maxwell-Stefan diffusivity. The latter is typically given in shape of a matrix, which increases the complexity of solving the equation with a rising number of species. Applying a mixture-average diffusion coefficient $D_{i,m}$ simplifies the calculation enormously. In a system with a total of Q species, this diffusion can be found using the mass fraction w_i of species i with

$$D_{i,m} = \frac{1 - w_i}{\sum_{j\neq i}^{Q} \frac{y_i}{D_{ij}}}. \tag{17}$$

A mixture-averaged multicomponent diffusion velocity $\boldsymbol{V}_{D,i}$ is then obtained with

$$\boldsymbol{V}_{D,i} = D_{i,m}\frac{\nabla w_i}{w_i} + D_{i,m}\frac{\nabla M_m}{M_m} + D_{i,T}\frac{\nabla T}{T} - z_i \mu_{i,m}\boldsymbol{E} + \sum_j \frac{M_j}{M_m} D_{j,m}\nabla x_j, \tag{18}$$

where M_m is the mean molar mass of the mixture, $D_{i,T}$ is the thermal diffusion coefficient, and the fourth term on the right hand side comes from the diffusion of ionic species in the case of electric fields, where $\mu_{i,m}$ is the mixture-averaged ion mobility. The fifth term on the right hand side is a mixture diffusion correction term. With the aforementioned equations and the density ρ, the diffusive flux vector $\boldsymbol{j}_i$ of species i is found as

$$\boldsymbol{j}_i = \rho w_i \boldsymbol{V}_{D,i}. \tag{19}$$

Using Einstein's relation to determine the mixture-averaged mobility

$$\mu_{i,m} = \frac{q}{k_B T} D_{i,m}, \tag{20}$$

the set of equations is complete to solve the single species balance equation

$$\rho\frac{\partial w_i}{\partial t} + \rho(\boldsymbol{u} \cdot \nabla) w_i = \nabla \cdot \boldsymbol{j}_i + R_i, \tag{21}$$

where the second term on the left hand side describes the change of the weight fraction of component i due to mass transport with the mass-averaged fluid velocity $\boldsymbol{u}$, and R_i represents a reaction term, summarizing all reactions that destroy or create component i.

The plasma chemistry is formulated on the basis of Refs. 24–27 and determines the power transfer from the electron fluid to the gas via electron impact collisions. However, it also considers heavy species

chemical reactions as well as surface-reactions. In Table I, a small set of the implemented reactions is shown with focus on the dissociation reactions responsible for the production of atomic hydrogen and those crucial for the estimation of the validity of the actinometry principle in the given discharge.[13] Reaction 10 is not specifically considered in the model but included in the cross section of reaction 1. However, we evaluate its reaction rate in the results section to determine if the actinometry principle can be applied at the conditions of the discharge at hand.

The most important channels for the destruction of atomic hydrogen at the pressures in the given discharge (~10 Pa) are surface recombination reactions. Volume recombination of atomic hydrogen is negligible as it requires a three-particle collision to carry away the liberated energy. Especially on metal surfaces like stainless steel, surface recombination occurs at high rates according to reaction 8.[10–12] Reaction 9 describes the recombination on the alumina dielectric of the plasma source, which happens at lower rates.

The production of atomic hydrogen is expected to happen predominantly through direct electron impact onto the ground-state molecule, which results in the nearly instantaneous dissociation when the molecule is excited to the H_2 $b^3\sum_u^+$ triplet state. In Ref. 28, this excitation is included as the most relevant in a total dissociation cross section, also considering dissociation through other triplet and singlet states with a threshold energy of 6 eV. Multi-step excitation can also lead to a significant contribution to dissociation reactions with reactions 2–4 being chosen for the plasma chemistry in the present work. There are also several heavy species volume reactions[27] included that lead to dissociation, but those are not listed in detail in Table I. Reaction 5 represents the ground-state excitation to the H (n = 3) state, for which the reaction rate is computed according to Eqs. (6) and (7) for the atomic hydrogen density measurement. Reactions 6 and 7 are two-step excitation processes, the rates of which have to be carefully assessed and compared to that of reaction 5 to confirm the validity of the actinometry approach, similar to reaction 13. Reactions 11 and 12 represent the radiative decay reactions that emit photons of the investigated wavelength in the actinometry experiment. Reactions 14 and 15 are considered as two-step excitation reactions with metastables that potentially compete with the ground-state excitation of argon in the contribution to the formation of the $Ar(^2p_1)$ state.

TABLE I. Some of the reactions used in the hydrogen plasma simulation.

No.	Reaction	Given as	References
1	$e + H_2 \rightarrow e + 2\,H$	$\sigma(\epsilon)$	28
2	$e + H_2(v1) \rightarrow e + 2\,H$	$\sigma(\epsilon)$	29
3	$e + H_2(v2) \rightarrow e + 2\,H$	$\sigma(\epsilon)$	29
4	$e + H_2(v3) \rightarrow e + 2\,H$	$\sigma(\epsilon)$	29
5	$e + H \rightarrow e + H(n = 3)$	$\sigma(\epsilon)$	30
6	$e + H(2s) \rightarrow e + H(n = 3)$	$\sigma(\epsilon)$	31
7	$e + H(2p) \rightarrow e + H(n = 3)$	$\sigma(\epsilon)$	31
8	$H \rightarrow 0.5\,H_2$	0.1 (metal)	11
9	$H \rightarrow 0.5\,H_2$	0.02 (Al_2O_3)	10
10	$e + H_2 \rightarrow e + H + H(n = 3)$	$\sigma(\epsilon)$	30
11	$H(n = 3) \rightarrow H(n = 2) + h\nu$	$4.41 \times 10^7\,s^{-1}$	32
12	$Ar(^2p_1) \rightarrow Ar(^1s_2) + h\nu$	$4.45 \times 10^7 s^{-1}$	33
13	$H(n = 4) \rightarrow H(n = 3) + h\nu$	$8.99 \times 10^6\,s^{-1}$	32
14	$e + Ar(^1s_3) \rightarrow e + Ar(^2p_1)$	$\sigma(\epsilon)$	34
15	$e + Ar(^1s_5) \rightarrow e + Ar(^2p_1)$	$\sigma(\epsilon)$	34

III. RESULTS

A. Experiments

Since the experiments serve the purpose of validation of the simulation, we compare atomic hydrogen concentrations as expected from simulation with measurements with corresponding operation parameters. The line intensities I_H and I_{Ar} are obtained as a time-average over an integration time of $t = 30$ s with the individual measurement points having exposure times of 3–30 ms based on the overall intensity of the discharge at the investigated angle. Only the intensity at the precisely given wavelengths (656.2–656.4 and 750.2–750.4 nm) is recorded for the evaluation. No saturation of the lines has been reached in any of the displayed results, and no radiation imprisonment is assumed. The characteristic emissions lines corresponding to the $Ar(^2p_5) \rightarrow Ar(^1s_4)$ de-excitation (751.465 nm) and the $Ar(^2p_4) \rightarrow Ar(^1s_4)$ de-excitation (747.117 nm) could, in theory, contribute to the measured 750.387 nm line due to the broad spectral resolution of the spectroscope. However, in the actinometry experiment, those lines could barely be distinct from background, which is probably caused by the low ground-state excitation cross sections of the respective upper states.[34] A background of the hydrogen plasma is subtracted from both emission line intensities. It is measured in a pure H_2 plasma at 750.387 nm at the same operation conditions as in the corresponding actinometry experiment.

The collimator optic allows probing the plasma at angles between 0° (aimed directly at the plasma source) and 14.6° with an uncertainty of ±0.5° at 0° and ±1° at larger angles, before facing the wall of the view port. The window is made from 3 mm borosilicate with a steady transmissivity to 500 and 1000 nm of about 91%. As this impacts the signal of both observed lines equally, it does not contribute to the uncertainty of the measurement. The plasma is operated at 20 Pa upstream pressure with ~3 vol. % Ar with slight, but accounted for, variations with the dissociation degree. From Eqs. (1), (3), and (4), all relevant sources of uncertainty of the measurement can be identified. First, no systemic uncertainty in the line signal ratio is expected as radiation imprisonment is assumed as negligible, and the window transmissivity is the same for both wavelengths. Second, the uncertainty in the estimated dissociation degree, the feed values of the calibrated mass flow controllers, and the gas-specific pumping speeds propagate into the Ar atom density calculation according to Eqs. (2) and (3). The latter two are incorporated into the total uncertainty, which mainly arises from the statistical uncertainty of the optic signal. The same can be said for the quenching correction factor, which has, anyway, only a small impact due to the low density in the discharge. The uncertainty in the excitation reaction rates, which depends on uncertainties in the plasma parameters, gas composition, EEDF shape, and collisional cross section, is not evaluated here. The uncertainty in the optic angle propagates into uncertainties in the assumptions of gas composition, plasma parameters, EEDF shape, and excitation reaction rates as well. However, the quantification of this effect is beyond the scope of this work.

The tuning of the plasma chemistry was performed operating the plasma at 20 Pa and 2.4 kW power input. To confirm its validity

beyond the tuned range, we tested several different power inputs down to 1.2 kW with reasonably good agreement. Figures 6(a) and 6(b) show the values of the atomic hydrogen molar fraction y_H over different optics angles pointing at the plasma. The dashed lines represent values taken from simulation, and the solid symbols are the actinometry measurements. We derive the uncertainty in the measurement solely from the statistical error of the experimental data. The values for y_H increase with the angle until a peak is reached and then drop off toward larger angles.

Especially for small angles, where the plasma intensity is brightest, a good match between simulation and experiment is reached. At 2.4 kW power, a maximum value of ~8% is reached for y_H, dropping off to 6% at the largest angle. We note that the offset between simulation and experiment increases toward lower powers and larger line of sight angles. The latter can be explained by the larger uncertainty in the calculation of the EEDF and reaction rates in the outer rings, where the electron temperatures drop off sharply. The simulation might underestimate the atomic hydrogen concentration at lower powers due to overestimation of the recombination coefficient. Two effects can potentially strengthen this effect: more vessel surface erosion and porosity at higher powers, yielding more surface for hydrogen atom adsorption and recombination and the lower atomic hydrogen density in the gas-phase reduces recombination rates by the Eley-Rideal mechanism.

To calculate the quenching reaction rates, we take the respective particle species density from a first estimate from simulation and the collision velocity as an average from the thermal velocities of the two colliding species. The cross sections are taken from Refs. 33–36. The actinometry principle can be applied if the ground-state excitation (reaction 5) dominates over the other reactions that produce the H (n = 3) state, the most relevant being reactions 6, 7, and 10. To confirm reaction 5 as predominant, we divide the rate of reaction 5 by the sum of the competing reaction rates. This is done for each ring and at each power, for which the validation is performed (1.2–2.4 kW plasma power) individually. Reaction 13 is excluded from this analysis as the H(n = 4) density is very low in the given discharge. The results are displayed in Fig. 7. One can see that the reaction rate for ground-state excitation stays larger than the sum of the other reaction rates throughout the complete tested range, except for the cases of 1.6 and 1.2 kW at large radial distance from the central plasma. However, due to the low electron temperatures in this region, the uncertainty in the EEDF becomes quite large, and the impact of the radiation from these rings on the integral intensity is negligible. Thus, one can conclude that ground-state excitation dominates over the other channels for production of the H(n = 3) state for all probed angles of the OES.

The two-step excitation processes of Ar according to reactions 14 and 15 have quite high rates in the given discharge. However, quenching by hydrogenic species is very efficient in depopulating the Ar metastables at rates at least 3 orders of magnitude larger than those of the two-step excitation processes.[35–41] Thus, we exclude two-step excitation processes through the Ar metastable states as significant contributors to the formation of the Ar(2p1) state.

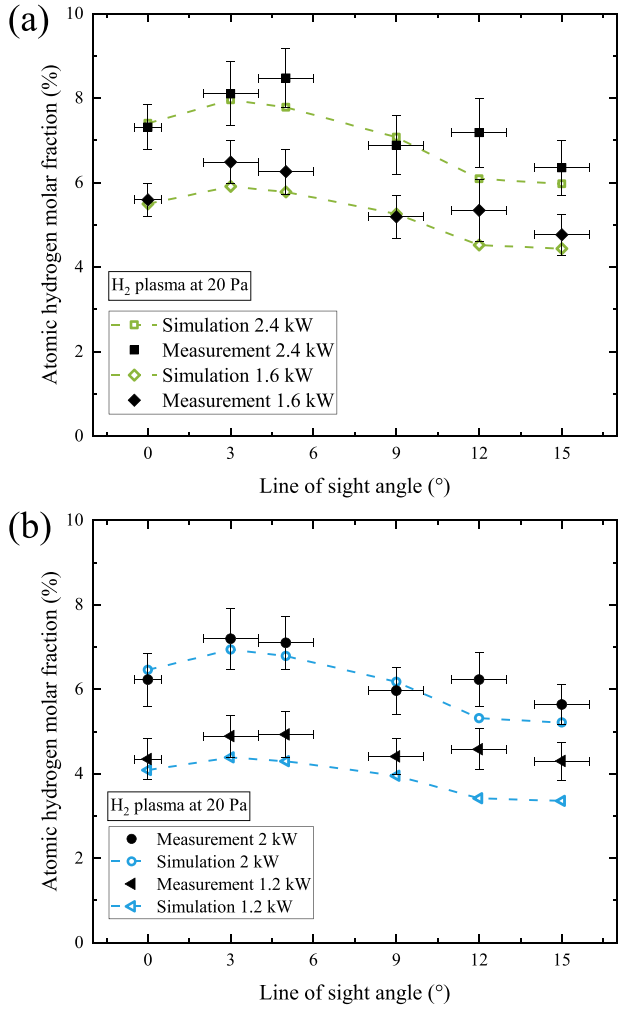

FIG. 6. Atomic hydrogen molar fractions as computed in simulation and measured experimentally for 1.6 and 2.4 kW in (a) and 1.2 and 2 kW in (b) over the line of sight angle, looking at the plasma.

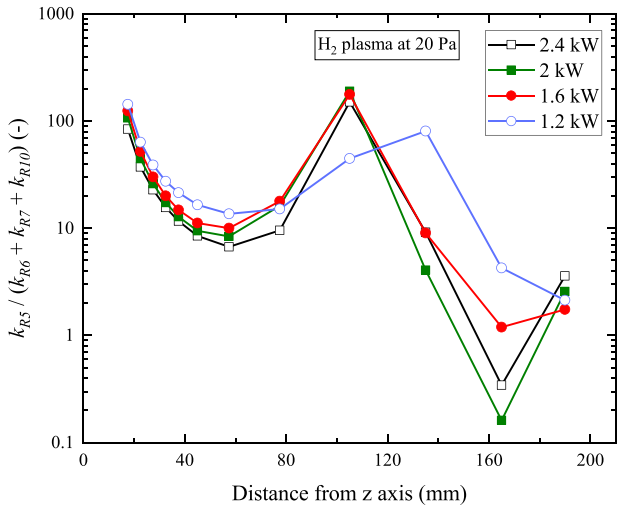

FIG. 7. Ratio of ground-state excitation to all relevant two-step excitation processes.

B. Simulation

The simulation provides valuable insights into the characterization of the cold plasma of the MFP. The electric field distribution, shown as calculated with the simulation in Fig. 8(a), resolves the regions of high power absorption by the electron fluid in the plasma. At the ends of the outer conductor and close to the plasma source, the electric field of the microwave rises, leading to significant electron heating at this location. This is also reflected in the calculated profiles of the electron temperature and density. Those play important roles in the production of atomic hydrogen, the duty of the plasma for application in the MFP, and are displayed in Figs. 8(b) and 8(c) for operation with 2.4 kW plasma power at 20 Pa. The forward, absorbed, and reflected microwave power are monitored to ensure no breakdown in the cooling air channel is simulated. As indicated by the electric field distribution, electron temperature and density rise highest at the ends of the plasma column. There, the cutoff electron density is reached, which causes a resonance of the microwave, leading to spikes in the electric field and very efficient heating of the electron fluid. Some measurements for the same type of plasma source are documented in Ref. 8. However, the reference is not suitable for a detailed comparison since the reported values were obtained using Ar. In our simulation, the peak electron densities reached are $\sim 1.4 \times 10^{17}$ m^{-3} up to several cm radial distance from the dielectric, dropping off $\sim$1 order of magnitude at larger radii of the vessel before approaching 0 in the plasma sheath. The electron temperature peaks at more than 7 eV close to the dielectric and reaches $\sim$2 eV in a large volume in the bulk of the plasma.

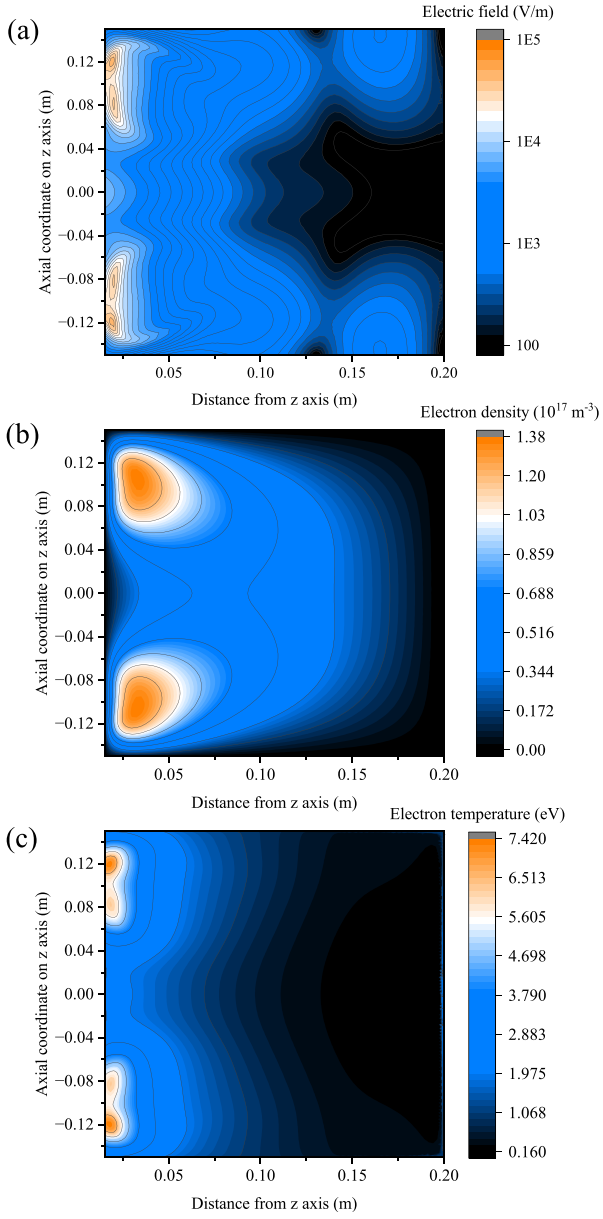

FIG. 8. Electric field distribution (a), electron density (b), and electron temperature (c) as computed by simulation in the plasma domain for operation with 2.4 kW plasma power at 20 Pa.

The change of electron temperature with pressure and power is revealed in a parametric study of the hydrogen plasma. The shown results are obtained by averaging along the z-axis for certain radial distances from the plasma source. Variation of pressure has quite significant changes on the radial profile of the electron temperature as depicted in Fig. 9(a). In this graph, the plasma power is fixed to 2.4 kW. We see that in this case, the peak temperature also only slightly increases toward lower pressures, but the profile becomes flatter, yielding larger electron temperatures throughout the whole plasma domain. The increased mean free path of the electrons at low pressures allows better propagation of the electron energy into the vessel before being depleted by collisions. This also increases the volume, in which a significant amount of dissociation reactions occurs. In Fig. 9(b), the pressure is set to 20 Pa, and power varied from 3 to 1 kW. We see that despite a threefold increase in power from 1 to 3 kW, the peak electron temperature only increases by $\sim$60% close to the plasma source. The radial profiles of the electron temperatures converge toward larger radii.

Judging by the atomic hydrogen molar fraction in the plasma, its production follows the distribution of electron temperature and density. Figure 10(a) shows the atomic hydrogen molar fraction throughout the vessel for a plasma operation at 2.4 kW and 20 Pa. One can see that the profile tailors that of the electron temperature, with the highest local concentrations close to the ends of the plasma source. Toward the plasma source dielectric, however, the concentration barely reduces, but toward the plasma vessel stainless steel walls, it drops off $< 1\%$ while reaching almost 30% peak values in the center. For the study of different pressures, we observe a similar trend as for the electron temperature. The radial profiles flatten even more toward lower pressures, but the peak concentration at the center barely increases.

The integral behavior is evaluated by determining the volume-averaged atomic hydrogen molar fraction for different powers and pressures. Figure 11(a) displays the change in y_H with power absorbed by the plasma in the simulation. Here, the pressure was fixed to 20 Pa. One can see that the atomic hydrogen molar fraction increases almost linearly with power within the observed range. This finding for the supply of atomic hydrogen is in good agreement with experimental measurements of the permeation flux changes with plasma power.[42] Figure 11(b) shows the trend of y_H with pressure. The simulation

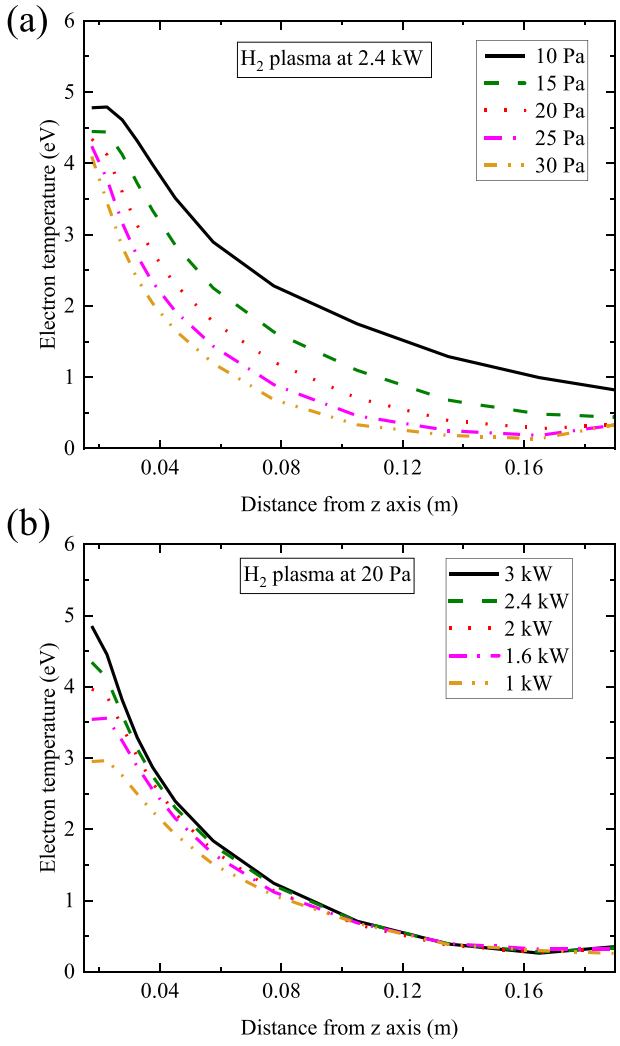

FIG. 9. Change of electron temperature in H2 plasma over the radial distance from the central axis of the plasma vessel with pressure (a) and power (b).

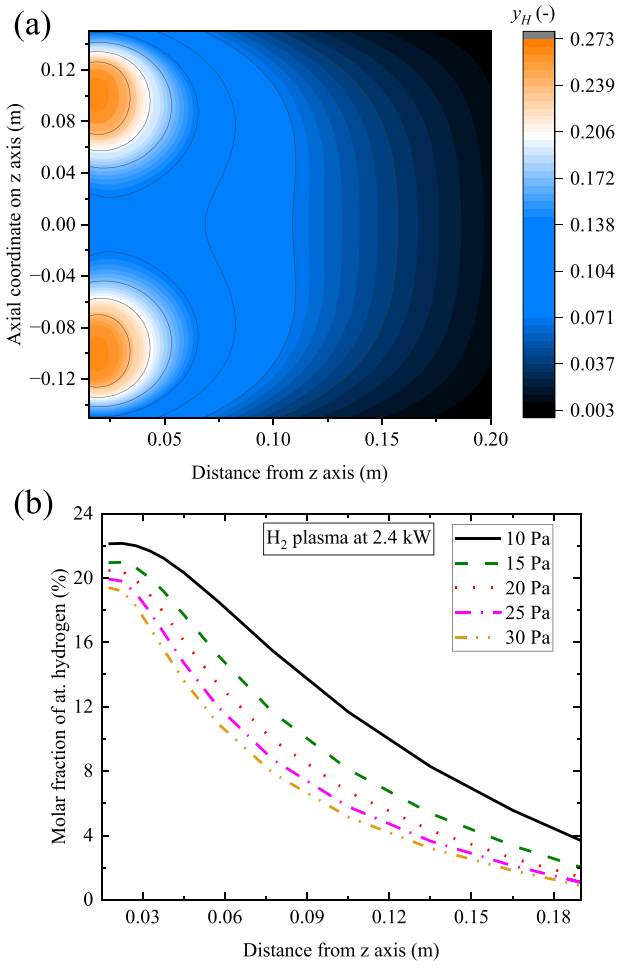

FIG. 10. Atomic hydrogen molar fraction over the plasma domain at 2.4 kW plasma power and 20 Pa in (a) and the radial profile of the atomic hydrogen molar fraction for pressures from 10 to 30 Pa at 2.4 kW plasma power in (b).

yields results from 40 to 10 Pa but does not reach convergence below that. This finding fits experimental observations because without magnetic field, the hydrogen plasma cannot build up the sufficient electron density corresponding to the cutoff to provide efficient heating in the resonance zone of the plasma.[8] In the MFP, the plasma is still expected to ignite below 10 Pa with the assistance of the PF coil magnetic field.[18] This is why, for extrapolation of y_H to pressures below 10 Pa, we used the green dashed line in Fig. 11(b). We see that the volume-average atomic hydrogen molar fraction is ∼5% at 20 Pa, ∼9% at 10 Pa, and ∼18% at 1 Pa, according to the fit function. The absorbed power by plasma did not deviate more than 0.62% from the 2.4 kW nominal value in the simulations.

C. Parameter extraction

The aim of the present work is to translate the plasma simulation results into a single excitation probability parameter such that the volume-averaged atomic hydrogen molar fractions correspond to those in the plasma in the experimental setup HERMES*plus*. The aforementioned data serve as benchmark for the evaluation of the excitation probabilities to match those to certain operation conditions.

A twin of the plasma simulation is modeled with no volume but only surface interactions. In this model, there are only ground-state and excited species. The former can become excited on the plasma source boundary with a probability p_{exc}. Excited particles can recombine on any walls according to the wall material's typical recombination coefficient. The plasma source diameter is set to 3 and 5 cm in two different parametric studies. The first value represents the plasma source diameter in the experiment and plasma simulation. A large-scale MFP for DEMO, however, requires significantly more power, which drives up the size of the plasma source conductors. The plasma source dielectric is, thus, assumed as 5 cm diameter in the MFP. Such an expansion of the surface for excitation causes large changes in the resulting excited particle production. This is displayed in Fig. 12(a), which shows the excited particle molar fractions obtained in the simplified model depending on the excitation probability on the plasma source

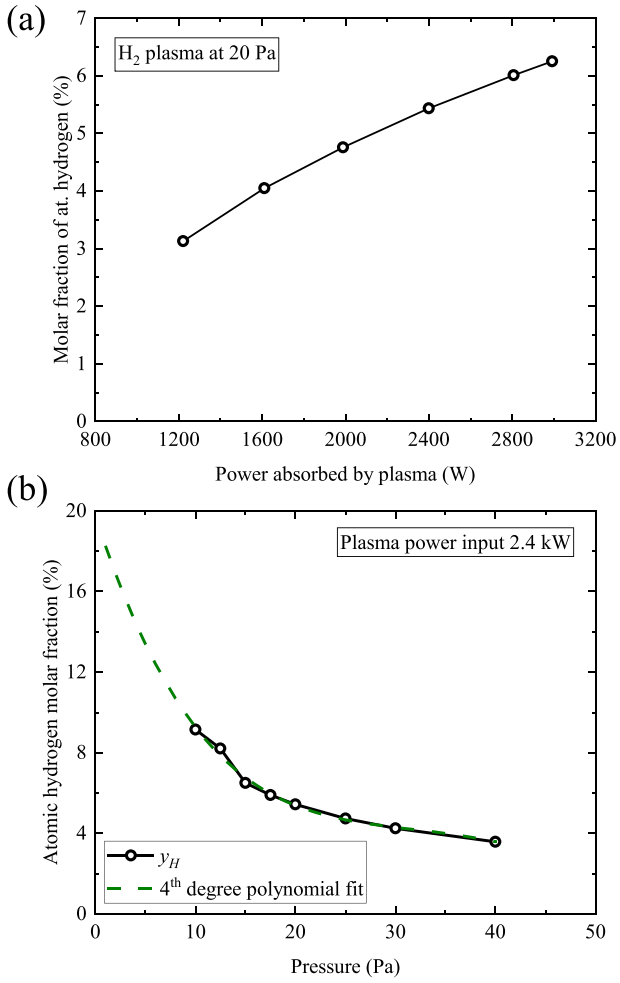

FIG. 11. Atomic hydrogen molar fraction over power (a) and pressure (b).

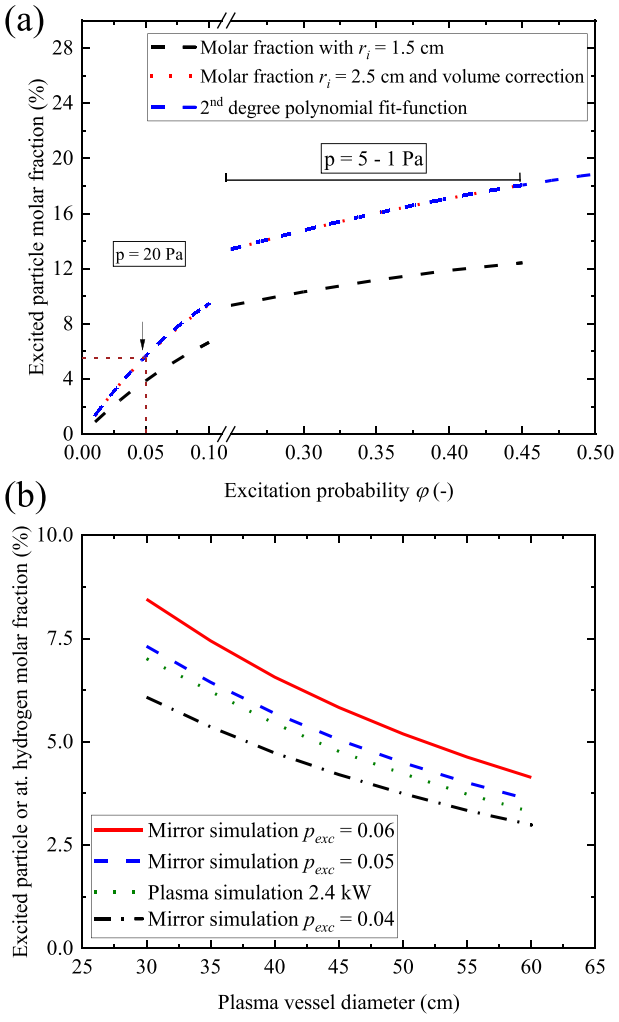

FIG. 12. Excited particle molar fraction of the excitation probability p_{exc} in (a) and excited particle or atomic hydrogen molar fraction over the plasma vessel diameter of the respective simulation model in (b).

boundary. The expanded plasma source yields significantly higher excited particle concentrations. To take the reduction in volume of the model by expansion of the plasma boundary into account, a volume-correction factor is introduced, which assumes a linear relationship between power density and excited particle molar fraction. Experiments on PDP fluxes have demonstrated this to be a reasonably accurate approximation.[42] The values to be used for the excitation in the TPMC simulation can be read from Fig. 12(a), taking the results in Fig. 11(b) into account. Thus, for the operation at 2.4 kW at 1 Pa, the atomic hydrogen molar fraction is expected at ∼18%, which is achieved with an excitation probability of 0.45 for a plasma source diameter of 5 cm.

The extrapolation for the atomic hydrogen molar fraction follows a fourth degree polynomial. In theory, the atomic hydrogen molar fraction should reach 100% as the pressure tends to 0 since less and less energy is required to dissociate the remaining quantity of hydrogen. Assuming that the plasma still burns and the microwave power is deposited, it should dissociate all of the remaining hydrogen. The fit-function underestimates y_H toward infinitesimally small pressures and, thus, delivers a conservative estimate of the atomic hydrogen molar fractions at pressures below 10 Pa. For the operation between 5 and 1 Pa with 2.4 kW, the corresponding excitation probabilities are roughly 0.25–0.45. A conservative limit for the operation at 10 Pa is an excitation probability of 0.1. To demonstrate that the choice of excitation probability is consistent for varying diameters of the plasma vessel, a parametric study of the diameter of the plasma vessel in both the validated plasma simulation and the mirror simulation is performed. Figure 12(b) shows the change in the molar fraction of atomic hydrogen or excited particles, respectively, with the diameter of the plasma vessel in both simulations. The calculated change with the plasma vessel diameter is the same for both simulations, proving that using the excitation probability on the plasma source surface is consistent with the results obtained in a complex plasma simulation.

IV. CONCLUSION

A workflow toward a development tool for a MFP in DEMO is introduced. We present a 2D axisymmetric plasma fluid simulation

that characterizes the plasma used to drive the permeation flux in an MFP. By use of optical emission spectroscopy, actinometry with argon is applied as experimental method to validate the plasma simulation within the operational range of plasma powers from 1.2 to 2.4 kW at 20 Pa pressure. The measured atomic hydrogen molar fraction ranges from ∼5% to 9% at the respective peak values of the radial profiles. The volume-averaged atomic hydrogen molar fraction is obtained with the validated simulation for pressures from 40 to 10 Pa, at which point it is determined as ∼9% and extrapolated down to 1 Pa, where it rises to ∼18%. A simplified version of the plasma simulation with no volume but only surface reactions and two gas species mimic the dissociation of hydrogen with interaction probabilities on the surfaces. By matching the atomic hydrogen concentration values of a certain plasma operation as obtained from the validated simulation to the results of the simplified model, an excitation probability is found that represents the plasma operation at certain conditions. This probability can be used in a Test Particle Monte Carlo approach vacuum simulation, which determines the MFP performance in view of pumping speed and hydrogen separation efficiency.

ACKNOWLEDGMENTS

This work has been carried out within the framework of the EUROfusion Consortium, funded by the European Union via the Euratom Research and Training Programme (Grant Agreement No. 101052200 — EUROfusion). Views and opinions expressed are, however, those of the author(s) only and do not necessarily reflect those of the European Union or the European Commission. Neither the European Union nor the European Commission can be held responsible for them.

This work has been done under the Tritium-Matter Injection-Vacuum Programme of the EUROfusion DEMO Project.

AUTHOR DECLARATIONS

Conflict of Interest

The authors have no conflicts to disclose.

Author Contributions

Yannick Kathage: Conceptualization (lead); Data curation (lead); Formal analysis (lead); Investigation (lead); Methodology (lead); Validation (lead); Visualization (lead); Writing – original draft (lead); Writing – review & editing (lead). **Stefan Hanke:** Investigation (supporting); Methodology (supporting); Project administration (equal); Supervision (equal); Writing – original draft (supporting); Writing – review & editing (supporting). **Thomas Giegerich:** Funding acquisition (supporting); Methodology (supporting); Project administration (equal); Resources (supporting); Software (supporting); Supervision (equal); Writing – review & editing (equal). **Christian Day:** Funding acquisition (lead); Methodology (supporting); Project administration (lead); Resources (lead); Supervision (lead); Writing – review & editing (equal).

DATA AVAILABILITY

The data that support the findings of this study are available from the corresponding author upon reasonable request.

REFERENCES

[1]T. Donné and W. Morris, see https://euro-fusion.org/wp-content/uploads/2022/10/2018_Research_roadmap_long_version_01.pdf for "European research roadmap to the realisation of fusion energy" (EUROfusion, 2018); accessed 18/08/2023.
[2]C. Day and T. Giegerich, "The direct internal recycling concept to simplify the fuel cycle of a fusion power plant," Fusion Eng. Des. **88**, 616–620 (2013).
[3]C. Day, K. Battes, B. Butler, S. Davies, L. Farina, A. Frattolillo, R. George, T. Giegerich, S. Hanke, T. Härtl *et al.*, "The pre-concept design of the DEMO tritium, matter injection and vacuum systems," Fusion Eng. Des. **179**, 113139 (2022).
[4]B. J. Peters, S. Hanke, and C. Day, "Metal foil pump performance aspects in view of the implementation of Direct Internal Recycling for future fusion fuel cycles," Fusion Eng. Des. **136B**, 1467–1471 (2018).
[5]A. I. Livshits, M. E. Notkin, and A. A. Samartsev, "Physico-chemical origin of superpermeability – Large-scale effects of surface chemistry on "hot" hydrogen permeation and absorption in metals," J. Nucl. Mater. **170**, 79–94 (1990).
[6]Y. Nakamura, A. Busnyuk, H. Suzuki, Y. Nakahara, N. Ohyabu, and A. Livshits, "Nb interaction with hydrogen plasma," J. Appl. Phys. **89**(1), 760–766 (2001).
[7]S. Hanke, C. Day, T. Giegerich, J. Igitkhanov, Y. Kathage, X. Luo, S. Varoutis, A. Vazquez Cortes, T. Härtl, and A. Busnyuk, "Progress of the R&D programme to develop a metal foil pump for DEMO," Fusion Eng. Des. **161**, 111890 (2020).
[8]W. Petasch, E. Räuchle, H. Muegge, and K. Muegge, "Duo-Pasmaline—A linearly extended homogeneous low pressure plasma source," Surf. Coat. Technol. **93**, 112–118 (1997).
[9]X. Luo and C. Day, "3D Monte Carlo vacuum modelling of the neutral beam injection system of ITER," Fusion Eng. Des. **85**, 1446–1450 (2010).
[10]L. St-Onge and M. Moisan, "Hydrogen atom yield in RF and microwave hydrogen discharges," Plasma Chem. Plasma Process. **14**(2), 87–116 (1994).
[11]M. Mozetic, M. Drobnic, and A. Zalar, "Recombination of neutral hydrogen atoms on AISI 304 stainless steel surface," Appl. Surf. Sci. **144-145**, 399–403 (1999).
[12]P. Kae-Nune, J. Perrin, J. Jolly, and J. Guillon, "Surface recombination probabilities of H on stainless steel, a-Si:H and oxidized silicon determined by threshold ionization mass spectrometry in H_2 RF discharges," Surf. Sci. **360**, L495–L498 (1996).
[13]A. Gicquel, M. Chenevier, K. Hassouni, A. Tserepi, and M. Dubus, "Validation of actinometry for estimating relative hydrogen atom densities and electron energy evolution in plasma assisted diamond deposition reactors," J. Appl. Phys. **83**, 7504–7521 (1998).
[14]A. Rousseau, A. Granier, G. Gousset, and P. Leprince, "Microwave discharge in H_2: Influence of H atom density on the power balance," J. Phys. D **27**, 1412–1422 (1994).
[15]Z. C. Geng, Y. Xu, X. F. Yang, W. G. Wang, and A. M. Zhu, "Atomic hydrogen determination in medium-pressure microwave discharge hydrogen plasmas via emission actinometry," Plasma Sources Sci. Technol. **14**, 76–82 (2005).
[16]R. Hippler, S. Pfau, M. Schmidt, and K. H. Schoenbach, *Low Temperature Plasma Physics: Fundamental Aspects and Applications* (Wiley-VCH, 2001).
[17]COMSOL, see https://doc.comsol.com/5.4/doc/com.comsol.help.plasma/PlasmaModuleUsersGuide.pdf for "COMSOL plasma module user's guide" (2018); accessed 30/05/2023.
[18]M. J. Druyvesteyn and F. M. Penning, "The mechanism of electrical discharges in gases of low pressure," Rev. Mod. Phys. **12**(2), 87–176 (1940).
[19]H. Khalilpour and G. Foroutan, "The effects of electron energy distribution function on the plasma sheath structure in the presence of charged nanoparticles," J. Plasma. Phys. **86**(2), 905860206 (2020).
[20]M. A. Lieberman and A. J. Lichtenberg, *Principles of Plasma Discharges and Materials Processing* (Wiley-Interscience, 2005).
[21]J. J. Scholtz, D. Dijkkamp, and R. W. A. Schmitz, "Secondary electron emission properties," Philips J. Res. **50**, 375–389 (1996).
[22]G. Lakits and H. Winter, "Electron emission from metal surfaces bombarded by slow neutral and ionized particles," Nucl. Instrum. Methods Phys. Res. **48**, 597–603 (1990).

[23]D. Bothe, "On the Maxwell-Stefan approach to multicomponent diffusion," in *Progress in Nonlinear Differential Equations and Their Applications* (Springer, 2011), Vol. 80, pp. 81–93.
[24]K. Hassouni, T. A. Grotjohn, and A. Gicquel, "Self-consistent microwave field and plasma discharge simulations for a moderate pressure hydrogen discharge reactor," J. Appl. Phys. **86**, 134–151 (1999).
[25]A. Obrusnik and Z. Bonaventura, "Studying a low-pressure microwave coaxial discharge in hydrogen using a mixed 2D/3D fluid model," J. Phys. D **48**, 065201 (2015).
[26]J. Giuliani, V. A. Shamamian, R. E. Thomas, J. P. Apruzese, M. Mulbrandon, R. A. Rudder, R. C. Hendry, and A. E. Robson, "Two-dimensional model of a large area, inductively coupled, rectangular plasma source for chemical vapour deposition," IEEE Trans. Plasma Sci. **27**(5), 1317–1328 (1999).
[27]C. D. Scott and M. Lefebvre, "Determining electron temperature and density in a hydrogen microwave plasma," J. Thermophys. Heat Transfer **10**(3), 426–437 (1996).
[28]L. H. Scarlett, J. K. Tapley, D. V. Fursa, M. C. Zammit, J. S. Savage, and I. Bray, "Electron-impact dissociation of molecular hydrogen into neutral fragments," Eur. Phys. J. D **72**(34), 1–8 (2018).
[29]L. H. Scarlett, J. S. Savage, D. V. Fursa, M. C. Zammit, and I. Bray, "Electron-impact dissociation of vibrationally-excited molecular hydrogen into neutral fragments," Atoms **7**(3), 75 (2019).
[30]L. L. Alves, "The IST-LISBON database on LXCat," J. Phys. Conf. Ser. **565**, 012007 (2014).
[31]I. Bray and A. T. Stelbovics, "Convergent close-couplin calculations of electron-hydrogen scattering," Phys. Rev. A **46**, 6995–7011 (1992).
[32]W. L. Wiese, M. W. Smith, and B. M. Glennon, *Atomic Transition Probabilities*, Hydrogen Through Neon Vol. 1 (National Standard Reference Data System, 1966).
[33]W. L. Wiese, J. W. Brault, K. Danzmann, V. Helbig, and M. Kock, "Unified set of atomic transition probabilities for neutral argon," Phys. Rev. A **39**(5), 2461–2471 (1989).
[34]O. Zatsarinny and K. Bartschat, "The B-spline R-matrix method for atomic processes: Application to atomic structure, electron collisions and photoionization," J. Phys. B **46**, 112001 (2013).
[35]J. Bittner, K. Kohse-höinghaus, U. Meier, and T. Just, "Quenching of two-photon excited H and O atoms by rare gases and small molecules," Chem. Phys. Lett. **143**(6), 571–576 (1988).
[36]N. Sadeghi, D. W. Setser, A. Francis, U. Czarnetzki, and H. F. Döbele, "Quenching rate constants for reactions of Ar atoms with 22 reagent gases," J. Chem. Phys. **115**, 3144–3154 (2001).
[37]N. Sadeghi and D. W. Setser, "Symmetry constraints in energy transfer between state-selected $Ar^*(^3P_2, {}^3P_0)$ metastable atoms and ground state H atoms," Chem. Phys. **95**, 305–311 (1985).
[38]A. Francis, U. Czarnetzki, H. F. Döbele, and N. Sadeghi, "Quenching of the 750.4 nm argon actinometry line by H_2 and several hydrocarbon molecules," Appl. Phys. Lett. **71**, 3796–3798 (1997).
[39]J. W. Lewis and W. D. Williams, "Collisional deactivation of atomic and molecular hydrogen," J. Quant. Spectrosc. Radiat. Transfer **16**, 939–946 (1976).
[40]L. G. Piper, J. E. Velazco, and D. W. Setser, "Quenching cross sections for electronic energy transfer reactions between metastable argon atoms and noble gases and small molecules," J. Chem. Phys. **59**, 3323–3340 (1973).
[41]A. Bogaerts and R. Gijbels, "Effects of adding hydrogen to an argon glow discharge: Overview of relevant processes and some qualitative explanations," J. Anal. At. Spectrom. **15**, 441–449 (2000).
[42]Y. Kathage, A. Vazquez Cortes, S. Merli, C. Day, T. Giegerich, S. Hanke, J. Igitkhanov, A. Schulz, and M. Walker, "Experimental progress in the development of a metal foil pump for DEMO," Plasma **6**(4), 714–734 (2023).